






Paleoclimate pattern effects help constrain climate sensitivity and 21st-century warming

Vincent T. Cooper^{a,1,2} , Kyle C. Armour^{a,b} , Gregory J. Hakim^a , Jessica E. Tierney^c , Natalie J. Burls^d , Cristian Proistosescu^e , Timothy Andrews^{f,g} , Wenhao Dong^{h,i,3} , Michelle T. Dvorak^b , Ran Feng^j , Matthew B. Osman^k, and Yue Dong^l 

Affiliations are included on p. 8.

Edited by Maria Rugenstein, Colorado State University, Fort Collins, CO; received May 6, 2025; accepted November 25, 2025 by Editorial Board Member Akkihebbal R. Ravishankara

Paleoclimates provide examples of past climate change that inform estimates of modern warming from greenhouse-gas emissions, known as Earth's climate sensitivity. However, differences between past and present climate change must be accounted for when inferring climate sensitivity from paleoclimate evidence. The closest paleoclimate analog to near-term warming from greenhouse-gas emissions is the Pliocene (5.3 to 2.6 Ma), a warm epoch with atmospheric CO₂ concentrations similar to today. Recent reconstructions indicate the Pliocene was 1 °C warmer than previously thought, implying higher climate sensitivity, which is also supported by recent reconstructions showing more cooling with reduced CO₂ at the Last Glacial Maximum (LGM; 19 to 23 thousand years ago). However, large-scale patterns of paleoclimate temperature change differ strongly from modern projections. Climate feedbacks and sensitivity depend on temperature patterns, and such “pattern effects” must be accounted for when using paleoclimates to constrain modern climate sensitivity. Here we combine data-assimilation reconstructions with atmospheric general circulation models to show Earth's climate is more sensitive to Pliocene forcing than modern CO₂ forcing. Pliocene ice sheets, topography, and vegetation alter patterns of ocean warming and excite destabilizing cloud feedbacks, and LGM feedbacks are similarly amplified by the North American ice sheets. Accounting for paleoclimate pattern effects produces a best estimate (median) for modern climate sensitivity of 2.8 °C and 66% CI of 2.4 to 3.4 °C (90% CI: 2.1 to 4.0 °C), substantially reducing uncertainty in projections of 21st-century warming.

climate dynamics | climate sensitivity | paleoclimate | cloud feedbacks | climate projections

The paleoclimate record constitutes a series of natural experiments providing fundamental insights into Earth's climate sensitivity. Using paleoclimate evidence to constrain the modern sensitivity to rising greenhouse-gas (GHG) concentrations requires accounting for differences in both climate forcings and feedbacks between past and modern climates (1–3). A key driver of such feedback differences across past climates is variation in the spatial pattern of sea-surface temperature, i.e., “paleoclimate pattern effects” (3). Pattern effects are variations in climate sensitivity and feedbacks that depend on spatial patterns of temperature change (e.g., refs. 4–8), and they arise in paleoclimates when non-GHG forcings (such as ice sheets, topography, and vegetation) affect large-scale temperature patterns. Paleoclimate pattern effects can have major impacts on estimates of modern climate sensitivity if non-CO₂ forcings strongly influence past temperature patterns, thereby producing climate feedbacks in the past that differ from those governing modern warming from GHG forcing (3).

The Pliocene (5.3 to 2.6 Ma) is the closest analog to near-term warming from GHG emissions (9). Its mid-Piacenzian warm period (3.3 to 3.0 Ma), hereafter “Pliocene,” is the most recent epoch with atmospheric CO₂ levels (near 400 ppm) similar to today (10). Pliocene warming thus provides an important constraint on the modern equilibrium climate sensitivity (ECS), the steady-state response of global-mean near-surface air temperature to a doubling of atmospheric CO₂ from preindustrial levels (2, 11). Previous assessments of Pliocene proxies report approximately 3 °C of global warming from preindustrial conditions and an upper bound of 4 °C (2, 11). However, recent reconstructions find a much warmer Pliocene with central estimates of 4 °C (12, 13). This revision to Pliocene warming suggests much higher ECS of 4.8 °C (12) and increased likelihood of the worst-case projections of 21st-century warming. Notably, high ECS of 4.8 °C has also been reported (14) based on recent reconstructions (15–17)

Significance

Climate sensitivity's uncertain upper bound determines the worst-case projections of global warming. Recent paleoclimate reconstructions suggest high sensitivity of 5 °C per CO₂ doubling. However, by analyzing spatial patterns of Pliocene warming—the closest analog to near-term warming—we show that ice sheets and topography amplified past warming through regional impacts on oceans and clouds. Similarly, the Last Glacial Maximum's cooling was amplified by ocean and cloud responses to massive ice sheets. Because these amplifying feedbacks are associated with paleoclimates' unique non-CO₂ forcings, the upper bound on modern warming from doubling CO₂ is reduced by 1 °C, constraining climate sensitivity to 2.1 to 4.0 °C (90% confidence). Thus paleoclimate evidence constrains climate sensitivity's upper bound and 21st-century warming projections.

PNAS policy is to publish maps as provided by the authors.

¹ Present address: Department of Earth, Atmospheric, and Planetary Sciences, Massachusetts Institute of Technology, Cambridge, MA 02139.

² To whom correspondence may be addressed. Email: vcooper@mit.edu.

³ Present Address: Department of Earth System Science, Ministry of Education Key Laboratory for Earth System Modeling, Institute for Global Change Studies, Tsinghua University, Beijing 100084, China.

This article contains supporting information online at <https://www.pnas.org/lookup/suppl/doi:10.1073/pnas.2511370123/-/DCSupplemental>.

Published January 22, 2026.

showing colder global-mean temperatures at the Last Glacial Maximum (LGM; 19 to 23 ka). But these globally resolved reconstructions tell us more than global means—they capture the spatial pattern of paleoclimate temperature change, and this spatial information is essential to constraining modern ECS.

To infer modern ECS from Pliocene evidence, we must consider differences in both forcing and feedbacks between the Pliocene and present climate. The Pliocene has both elevated GHG levels (10, 18) as well as additional forcing from i) reduced ice sheets over West Antarctica and Greenland, ii) increased vegetation, especially over northern high latitudes, and iii) changes in land-sea distribution (1, 2, 19, 20). Previous work found that the Pliocene’s global-mean warming is mostly attributable to CO₂ (21–23). However, modeling studies show that the non-CO₂ forcings drive distinct climate responses especially at regional scales (e.g., refs. 21 and 23–28), and that Pliocene temperature patterns may differ substantially from those in response to modern CO₂ forcing (24), thereby producing different climate feedbacks. Accounting for such pattern effects in cold-period evidence from the LGM leads to stronger constraints on modern ECS (3). The key question addressed here is: would accounting for Pliocene pattern effects also strengthen constraints on modern ECS?

We quantify Pliocene pattern effects by synthesizing proxy data with climate models, and we use these results to revise estimates of modern ECS and 21st-century warming. Spatially complete reconstructions of the Pliocene (12, 13) from paleoclimate data assimilation (15, 16, 29) are used in numerical simulations with five atmospheric general circulation models (AGCMs) to quantify relationships between temperature patterns and climate feedbacks (e.g., refs. 3 and 5). We analyze differences between feedbacks in the Pliocene compared to modern warming from CO₂. We then combine our Pliocene results with an investigation of the LGM (3), and we quantify the impacts of the feedback differences on estimates of modern ECS and projections of 21st-century warming.

Overview of Paleoclimate Pattern Effects and ECS

Modern ECS, climate feedbacks, and paleoclimate pattern effects are related through the global-mean energy balance,

$$\Delta N = \Delta F + \lambda \Delta T, \quad [1]$$

where ΔN is the change in top-of-atmosphere radiative balance; ΔF is the “effective” radiative forcing, i.e., the change in net downward radiative flux after atmospheric adjustments to imposed perturbations, excluding radiative responses to changing surface temperature (11); λ is the net climate feedback (negative for stable climates); and ΔT is the change in near-surface air temperature. All values are global means, and differences (Δ) are relative to the preindustrial baseline. When the forcing is a doubling of preindustrial CO₂ concentrations (2xCO₂), and the climate reaches equilibrium ($\Delta N = 0$), the resulting ΔT is the modern ECS:

$$\text{ECS} = -\Delta F_{2x\text{CO}_2} / \lambda_{2x\text{CO}_2}, \quad [2]$$

where $\Delta F_{2x\text{CO}_2}$ is the effective radiative forcing and $\lambda_{2x\text{CO}_2}$ is the net feedback from modern CO₂ doubling. Increasingly negative values of λ indicate more-stable climates and lower ECS.

Paleoclimate pattern effects ($\Delta\lambda$) are quantified as the difference between $\lambda_{2x\text{CO}_2}$ and a paleoclimate feedback, e.g., the

Pliocene feedback (λ_{plio}), due to differences in the spatial patterns of warming:

$$\Delta\lambda = \lambda_{2x\text{CO}_2} - \lambda_{\text{plio}}. \quad [3]$$

$\Delta\lambda$ also can vary with global-mean temperature (e.g., refs. 2, 3, and 30). However, this temperature dependence can be omitted for the Pliocene due to similar levels of global warming from Pliocene and 2xCO₂ forcings (2), and it is relatively small for LGM levels of global cooling (3, 31).

Modern ECS and $\lambda_{2x\text{CO}_2}$ can be constrained by estimating λ_{plio} and $\Delta\lambda$, then combining Eqs. 2 and 3:

$$\text{ECS} = -\Delta F_{2x\text{CO}_2} / (\lambda_{\text{plio}} + \Delta\lambda). \quad [4]$$

$\Delta\lambda$ depends on spatial patterns of Pliocene temperature anomalies, for which we use state-of-the-art reconstructions from data assimilation (12, 13) as boundary conditions for simulations using five AGCMs, as described in the following section.

Pliocene Pattern Effects from Data Assimilation

Patterns of Pliocene Sea-Surface Temperature. In Fig. 1, we compare the projected sea-surface temperature (SST) anomalies from modern 2xCO₂, based on the multimodel mean of quasi-equilibrium simulations in LongRunMIP (32), with the various Pliocene reconstructions from “plioDA” (12) and ref. 13 that we use to quantify Pliocene pattern effects. The Pliocene patterns include the best estimates from plioDA (12) and ref. 13, as well as alternative plioDA reconstructions that test structural uncertainty and endmembers of the plioDA ensemble (Fig. 1 and *SI Appendix*, Figs. S1–S4) (*Materials and Methods*).

The paleoclimate reconstructions use data assimilation (e.g., refs. 15, 16, 29, and 33–35), which optimally combines dynamical constraints from climate models with observational constraints from proxy data. In brief, the method begins with a “model prior,” i.e., a distribution of possible climate states defined by an ensemble of simulations in coupled climate models. Proxy data are then evaluated against the prior, which updates the prior according to the prior’s covariance structure, weighting the relative errors in the proxies and the prior. The final result is a posterior distribution of climate states constrained by the data and the models’ dynamics. The best estimate of the state is the reconstruction’s ensemble mean, while its ensemble members sample the uncertainty. A reconstruction’s results depend on specific aspects of the methods, model priors (36), and observations.

To address reconstruction uncertainty, we analyze pattern effects across a wide range of possible Pliocene temperature patterns that use different assimilation methods, model priors, and subsets of proxy data. Focusing on sensitivity to the model prior, the “PlioMIP2 Prior” version of plioDA uses 14 PlioMIP2 simulations (37) to inform its prior. The “Perturbed Cloud Prior” uses 21 simulations that are designed to capture Pliocene temperature gradients by substantially altering models’ cloud physics instead of changing the paleoenvironmental boundary conditions (38–40). Focusing on sensitivity to the proxy network, the “PlioVar Data” version restricts data to the KM5c interglacial (41), and we also test endmembers of the plioDA ensemble (*SI Appendix*, Fig. S4) (*Materials and Methods*). Ref. 13 and plioDA (12) have partially overlapping proxy networks, model priors (both best estimates include simulations from PlioMIP2), and assimilation methods (ensemble Kalman filter); however, there are substantial differences between the two reconstruction efforts

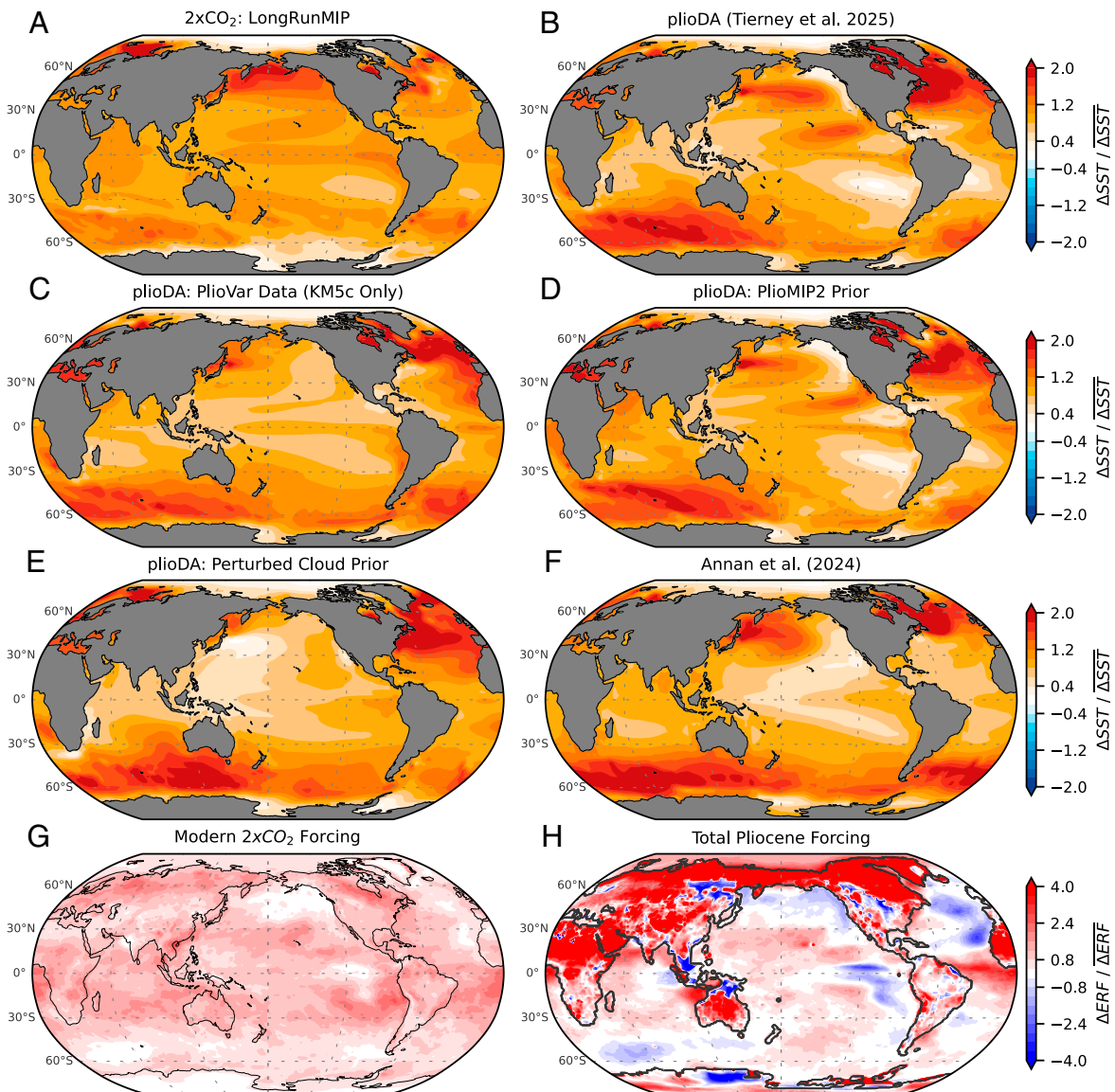


Fig. 1. Patterns of sea-surface temperature (SST) anomalies and effective radiative forcing (ERF). (A) Multimodel mean of modern SST response to $2xCO_2$ in quasi-equilibrium simulations from LongRunMIP (32). (B–F) Data-assimilation reconstructions from: (B) plioDA best estimate (12); alternative plioDA using (C) only the PlioVar proxy data representing the KM5c interglacial, (D) only the PlioMIP2 prior, or (E) only the perturbed-cloud prior; and (F) best estimate from ref. 13. ERF from (G) modern $2xCO_2$ and (H) Pliocene total forcing, including greenhouse gases, reduced Greenland and Antarctic ice sheets, sea level, topography, and vegetation (24). All panels show annual-mean anomalies, and local values are divided by global means. Pliocene SSTs are infilled to modern coastlines.

in terms of the proxies included, model priors, and methods (e.g., forward modeling of proxies in plioDA) that lead to differences in their results (12) (Fig. 1 B and F).

Despite the substantial uncertainty in the details of the Pliocene SST patterns shown in Fig. 1, the reconstructions all have two common features that distinguish the Pliocene from the modern response to $2xCO_2$: the Pliocene has amplified SST warming in the Southern Ocean and the North Atlantic Ocean (Fig. 1 and SI Appendix, Fig. S1). The distinct Pliocene warming pattern is driven by the distinct spatial pattern of Pliocene forcing (Fig. 1H) (24), which arises from the Pliocene’s non- CO_2 forcings (changes in ice sheets, topography, and vegetation) and differs substantially from the relatively uniform forcing produced by CO_2 alone (Fig. 1G). We note that the Bering Strait is closed in Fig. 1H following refs. 20, 37, and 42, although geological evidence suggests the Bering Strait began opening prior to the Pliocene (43). Importantly, the SST reconstructions show

amplified warming in the North Atlantic Ocean because of the proxy data, and that result is not sensitive to models’ Bering Strait configuration (12). The connection between the non- CO_2 Pliocene forcings and the SST patterns they produce has been demonstrated in coupled climate models (24), which we return to in the Discussion.

Quantifying Feedbacks and Pattern Effects. We estimate the net climate feedback, λ , for each warming pattern in Fig. 1 using AGCM simulations with prescribed SST and sea-ice concentration (SIC) (Materials and Methods). Following ref. 3, we begin with a control simulation using the preindustrial “baseline” pattern (16). We repeat the AGCM simulations, changing only the SST and SIC to the $2xCO_2$ pattern from LongRunMIP (Fig. 1A) and to each of the Pliocene patterns (Fig. 1 B–E; SIC in SI Appendix, Figs. S2–S4). We hold the forcings constant at modern levels across all simulations to

isolate the radiative response to changes in surface temperature (*Materials and Methods*). For each simulation, we calculate ΔN and ΔT relative to the preindustrial baseline, and the net feedback is $\lambda = \Delta N / \Delta T$ from Eq. 1 with $\Delta F = 0$.

In Fig. 2, we compare λ_{2xCO_2} with λ_{Plioc} and quantify Pliocene pattern effects ($\Delta\lambda$). In all five AGCMs, λ_{Plioc} is more positive (meaning more amplifying and less stable) than λ_{2xCO_2} , indicating that the climate system is more sensitive to Pliocene forcing than it is to modern $2xCO_2$ forcing. We test whether this result is robust despite uncertainties in atmospheric model physics and Pliocene reconstructions by running the simulations with CAM4, CAM5, CAM6, GFDL-AM4, and HadGEM3-GC3.1-LL, and by testing three different Pliocene patterns (Fig. 1 B, D, and F) with all five AGCMs. We test additional Pliocene patterns, including the 5th and 95th percentiles of the plioDA ensemble (*SI Appendix, Fig. S4*), with CAM4 and CAM5 (*Materials and Methods*). Despite the uncertainties in Pliocene SST patterns and atmospheric model physics, there is a clear Pliocene pattern effect with $\Delta\lambda < 0$ (Fig. 2B), albeit with uncertain magnitude.

In summary, the Pliocene warming pattern excites more-positive (more-amplifying) climate feedbacks compared to the $2xCO_2$ warming pattern ($\lambda_{Plioc} > \lambda_{2xCO_2}$), i.e., the Pliocene pattern effect is negative ($\Delta\lambda < 0$). As will be shown below, the negative pattern effect indicates that positive feedbacks amplifying Pliocene warming do not play an equivalent role in the modern climate's response to greenhouse-gas forcing. Accounting for this negative Pliocene pattern effect would lead to lower estimates of modern ECS and future warming (Eq. 4) (3).

Mechanisms Responsible for Pliocene Pattern Effects. To diagnose the mechanisms contributing to more-positive climate feedbacks in the Pliocene, we first use radiative kernels to assess each component feedback within the AGCM simulations. Kernels are precomputed sensitivities of radiative fluxes to perturbations in temperature, water vapor, and surface albedo, enabling efficient estimation of various feedbacks (*Materials and Methods*) (44). We find that the cloud feedback (λ_{cloud}), namely the shortwave component associated with low clouds, is the dominant driver of $\lambda_{Plioc} > \lambda_{2xCO_2}$ (*SI Appendix, Figs. S5 and S6*). The combined lapse-rate and water-vapor feedbacks make an additional contribution to more-positive λ_{Plioc} (*SI Appendix, Fig. S5*). Next, we inspect the spatial distribution of the Pliocene's more-positive cloud feedbacks to understand their source.

In Fig. 3, we compare the spatial patterns of λ_{cloud} in the Pliocene versus $2xCO_2$. The most pronounced differences are over the Southern Ocean (Indian sector) and the North Atlantic. The zonal mean of $\Delta\lambda_{cloud}$ (Fig. 3A) illustrates that the Pliocene's extratropical cloud feedbacks are responsible for $\lambda_{Plioc} > \lambda_{2xCO_2}$, supported by extratropical lapse-rate feedbacks (*SI Appendix, Fig. S9*). Comparing Fig. 3's λ_{cloud} with Fig. 1's SST patterns (zonal mean SST in *SI Appendix, Fig. S10*), we see that the regions with amplified Pliocene SST anomalies are approximately collocated with the amplified Pliocene λ_{cloud} . That is, amplified SST anomalies in the extratropics are responsible for more-positive feedbacks in the Pliocene, which is consistent with a similar analysis of the Last Glacial Maximum (3). When SST warming is strongly amplified in the extratropics compared to the SST warming in tropical regions of atmospheric deep convection (e.g., the west Pacific warm pool), tropospheric stability is decreased and low-cloud cover is reduced, which is a positive feedback on the initial warming (3, 7, 45). Past studies of the Pliocene emphasize the zonal SST in the tropical Pacific and meridional temperature gradients (12, 22, 46–50), while we find that the amplification of warming in the North Atlantic and especially the Southern Ocean are the dominant features that distinguish Pliocene feedbacks from the modern response to $2xCO_2$.

The final and essential aspect of the mechanism is that amplified warming in the Southern Ocean and North Atlantic is due to non- CO_2 forcings (ice sheets, vegetation, and topography), as shown in *SI Appendix, Fig. S11*. This attribution has been illustrated by simulations in coupled climate models that separate the SST response to Pliocene CO_2 versus non- CO_2 forcings (e.g., refs. 21, 23, 24, and 37). Pliocene warming in the North Atlantic is amplified by closure of Arctic ocean gateways through changes in the Atlantic Meridional Overturning Circulation (AMOC) (e.g., refs. 25, 51, and 52), reductions in ice sheets (27), and vegetation changes (21). Further investigation of the Bering Strait's role is warranted given its openings before and after the Pliocene (e.g., ref. 43). Amplified warming in the Southern Ocean is associated with the reduced Antarctic Ice Sheet and topography through changes in ocean circulation (24, 53). While amplified warming of the Southern Ocean appears in all reconstructions (Fig. 1), its magnitude is uncertain due to sparse proxy data, and this uncertainty makes a large contribution to our spread in $\Delta\lambda$ (*SI Appendix, Figs. S8–S10*). We also note that the Southern Ocean continues to warm on the millennial timescale in LongRunMIP's CO_2 -forcing simulations (32), and the true equilibrium response to CO_2 forcing is uncertain. More work is needed to understand how much of the Pliocene's warming pattern is directly attributable to the equilibrated response to CO_2 versus non- CO_2 forcing. LGM reconstructions, however, do not show a Pliocene-like amplification in the Southern Ocean

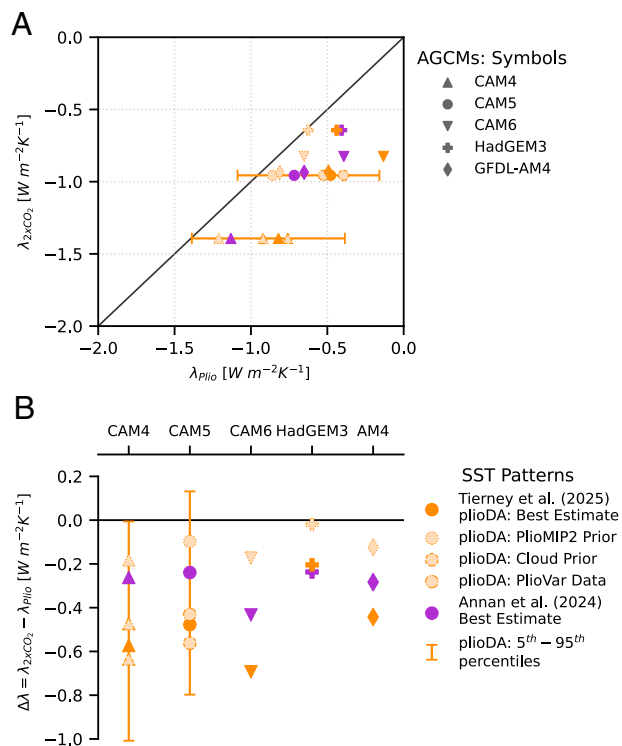


Fig. 2. Quantification of the Pliocene pattern effect ($\Delta\lambda$). Note that each legend applies to both panels; different atmospheric general circulation models (AGCMs) are denoted by symbols, and different Pliocene warming patterns are denoted by colors and borders. (A) Scatter plot of net climate feedbacks (λ), showing λ_{2xCO_2} versus λ_{Plioc} , for each AGCM and Pliocene pattern, with $\lambda_{2xCO_2} = \lambda_{Plioc}$ shown as solid line. (B) Pliocene pattern effect, $\Delta\lambda = \lambda_{2xCO_2} - \lambda_{Plioc}$, using values in panel (A). Error bars for plioDA represent endmembers of the ensemble reconstruction (*Materials and Methods*).

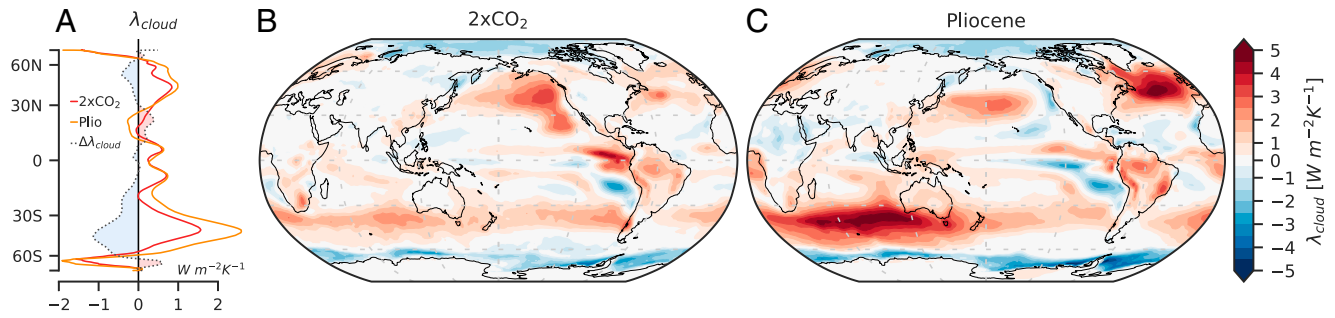


Fig. 3. Cloud feedbacks from modern $2\times\text{CO}_2$ forcing versus Pliocene warming. (A) Zonal means of panels B and C, and their difference, $\Delta\lambda_{\text{cloud}}$; negative values of $\Delta\lambda_{\text{cloud}}$ contribute to the negative Pliocene pattern effect. (B and C) Spatial distributions of cloud feedbacks, $\lambda_{\text{cloud}} = \Delta N_{\text{local}}/\Delta T$, where ΔN_{local} is the local anomaly in top-of-atmosphere radiation attributable to cloud feedbacks (estimated with radiative kernels), and ΔT is the global-mean T anomaly. Multimodel mean of (B) λ_{cloud} using the LongRunMIP $2\times\text{CO}_2$ pattern and (C) multipattern mean λ_{cloud} from Pliocene patterns in Fig. 1 B, D, and F (plioDA best estimate (12), alternative plioDA using only the PlioMIP2 prior, and ref. 13 best estimate; these patterns were tested in all atmosphere models). All panels show multimodel means across atmosphere models.

(3), suggesting that the long-timescale direct response to CO_2 is not the key driver of the Pliocene pattern in the Southern Ocean. Compared to coupled models' Pliocene simulations, both the North Atlantic and Southern Ocean SST features are even more pronounced in data-assimilation reconstructions constrained by paleoclimate proxies (Fig. 1) (12, 13). Thus coupled models are essential for illustrating mechanisms of paleoclimate pattern effects, and incorporating observational constraints through data assimilation is key to producing reliable SST patterns and constraining $\Delta\lambda$.

While our comparison of the Pliocene versus modern $2\times\text{CO}_2$ uses the LongRunMIP pattern (32), we note that there is substantial uncertainty in the projected SST pattern from $2\times\text{CO}_2$. However, because Pliocene and LGM pattern effects arise from how non- CO_2 forcings shape paleoclimate temperature patterns, we expect conclusions about $\Delta\lambda$ to be relatively insensitive to uncertainty in the SST pattern from CO_2 forcing. Furthermore, ref. 54 finds that the feedback uncertainty from CO_2 -forced SST patterns is only 10% of the total feedback spread across different models. That result emphasizes the importance of using multiple atmospheric models to quantify $\Delta\lambda$ and that the feedback spread from CO_2 -forced patterns is small compared to that arising from the Pliocene reconstructions. We test whether results are sensitive to the $2\times\text{CO}_2$ pattern and find this uncertainty does not affect the conclusions (Materials and Methods).

In summary, non- CO_2 forcings from Pliocene ice sheets, topography, and vegetation altered the spatial pattern of ocean warming, in turn producing positive cloud feedbacks in the extratropics that strongly amplified global warming during the Pliocene (Fig. 3). Because of these amplifying feedbacks, more of the Pliocene warming was caused by non- CO_2 forcings than previously thought, meaning that less warming is attributable to elevated CO_2 alone. Since these amplifying feedbacks from non- CO_2 forcing do not play a role in the modern response to $2\times\text{CO}_2$ alone, we now show that accounting for the Pliocene pattern effect lowers estimates of modern ECS and reduces the likelihood of worst-case projections for 21st-century warming.

Modern Climate Sensitivity and 21st-Century Warming

To constrain modern ECS with paleoclimate evidence, we first infer climate feedbacks during a paleoclimate period from changes in Earth's energy budget, and then we account for

differences relative to the modern response to $2\times\text{CO}_2$ (1–3). Measures of climate sensitivity depend on the timescale of interest, and we follow ref. 2, hereafter “SW20,” in focusing on the 150-y timescale of “effective” climate sensitivity (S), and in treating slow paleoclimate feedbacks, e.g., ice sheets, as radiative forcings (1).

First, we estimate λ_{plio} by applying Eq. 1 to the Pliocene (Materials and Methods). We update ΔT_{plio} from SW20's values of 3.0 ± 1.0 °C (1σ) to plioDA's result of $\Delta T_{\text{plio}} = 4.1 \pm 0.6$ °C (1σ). We also update the non-GHG (greenhouse gas) effective radiative forcing to $\Delta F_{\text{NonGHG}} = 1.7 \pm 1.0$ (1σ) W m^{-2} (24). Given that $\Delta F_{\text{GHG}} \approx 2.2$ W m^{-2} (2, 24), we have a central estimate of total $\Delta F_{\text{plio}} = 3.9$ W m^{-2} and $\lambda_{\text{plio}} \approx -1.0$ $\text{W m}^{-2} \text{K}^{-1}$ (Materials and Methods).

The key update to modern ECS constraints in this study is the inclusion of paleoclimate pattern effects for the Pliocene ($\Delta\lambda$; Eqs. 3 and 4) and the synthesis with pattern effects for the Last Glacial Maximum (3). We combine uncertainty across SST patterns and atmospheric models (Fig. 2; Materials and Methods), which produces a central estimate for Pliocene pattern effects of $\Delta\lambda = -0.37 \pm 0.32$ (1σ) $\text{W m}^{-2} \text{K}^{-1}$. We adapt the Bayesian framework of SW20 to include Pliocene $\Delta\lambda$, following ref. 3 (Materials and Methods).

In Fig. 4A, we show the S likelihoods from Pliocene evidence alone. For comparison, we include the original SW20 results and the likelihood with updated Pliocene global-mean ΔT and ΔF_{NonGHG} but excluding Pliocene pattern effects. As seen in Fig. 4A, the updates from the global-mean information alone (excluding $\Delta\lambda$) suggest a much higher ECS (12). However, the spatial information in the Pliocene reconstructions—quantified as $\Delta\lambda$ —has a larger and opposite impact. Including $\Delta\lambda$ shifts the maximum likelihood from 3.7 °C to 2.7 °C and substantially reduces the high tail of the distribution.

We now revise the best estimate for modern ECS by combining the Pliocene with the additional lines of evidence in SW20: the Last Glacial Maximum (LGM), the historical record (c. 1870–present), and process understanding (Materials and Methods) (Fig. 4B). We first show SW20's results, then we include paleoclimate updates only to global-mean quantities (i.e., excluding $\Delta\lambda$), which increases ECS substantially. We then include $\Delta\lambda$ from only the Pliocene or LGM (3), and finally we combine our results for Pliocene and LGM $\Delta\lambda$ to provide a best estimate that fully accounts for paleoclimate pattern effects and their uncertainties. Once again, global-mean paleoclimate

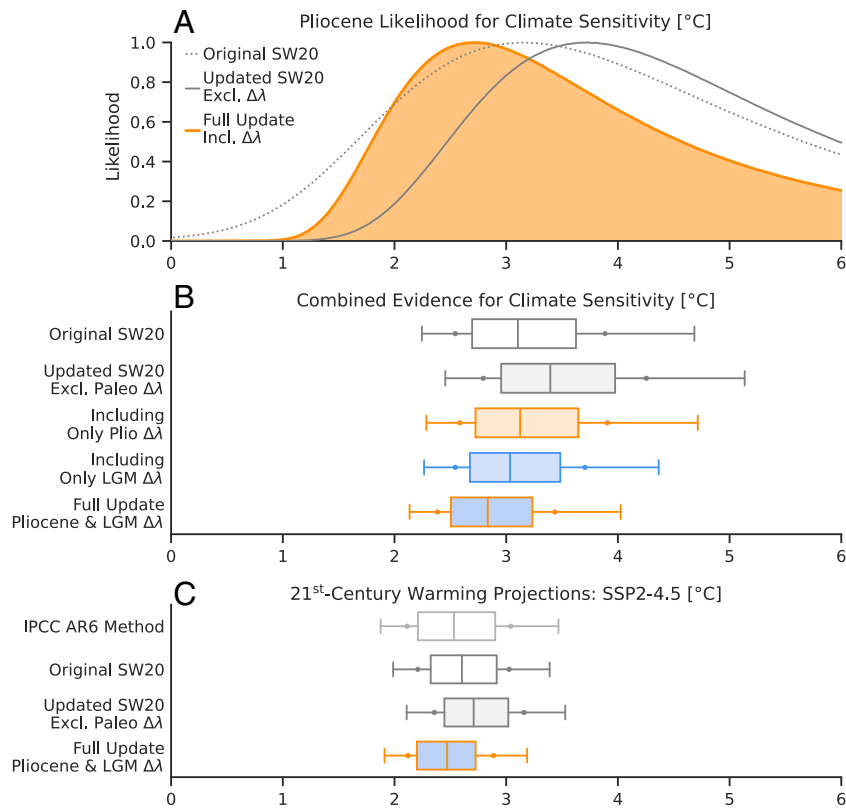


Fig. 4. Modern climate sensitivity and 21st-century warming, accounting for paleoclimate pattern effects ($\Delta\lambda$). (A) Pliocene-only likelihoods (dotted) from SW20 (2); (gray) including updates to ΔT_{Plio} and ΔF_{Plio} but excluding pattern effects; (orange) fully updated SW20 including $\Delta\lambda$. (B) Posterior probability density functions (PDFs) after combining lines of evidence: (gray, white fill) SW20, (gray, gray fill) SW20 with updated paleoclimate ΔT and ΔF but excluding $\Delta\lambda$, (orange) including $\Delta\lambda$ only for the Pliocene, (blue) $\Delta\lambda$ only for the Last Glacial Maximum (LGM) (3), and (orange, blue fill) Full Update including Pliocene and LGM $\Delta\lambda$. Panels (A and B) show effective climate sensitivity (S), as in SW20. (C) Projected global warming from the FaIR model (55), measured as mean anomaly over 2081–2100 relative to 1850–1900 mean, using climate sensitivity distribution from IPCC AR6 (11), then using three distributions corresponding to panel (B): SW20, updated SW20 excluding paleoclimate $\Delta\lambda$, and the Full Update. Line caps indicate 5th to 95th percentiles, dots indicate 66% *likely* range, box indicates 25th to 75th percentiles, and line indicates median.

updates increase ECS, but the spatial information from pattern effects is more impactful and leads to much stronger overall constraints, particularly for the upper bound. The revised best estimate (median) for modern ECS becomes 2.8 °C, with a 66% range of 2.4 to 3.4 °C (90% CI: 2.1 to 4.0 °C) (Fig. 4B and *SI Appendix*, Table S3). This range represents a major update to the upper bounds in SW20 (2) and the IPCC Sixth Assessment report (AR6) (11), while our lower bound confirms those assessments. For comparison with SW20's robustness tests, we find a 66% robust range of 2.6 to 3.8 °C (90% CI: 2.3 to 4.6 °C), which also represents a much stronger constraint compared to the 95th percentile of 5.7 °C in SW20's robust range.

Importantly, our updates to modern ECS also reduce uncertainty in projections of 21st-century warming. Fig. 4C shows the 2081–2100 mean warming relative to 1850–1900 projected by the FaIR model (55), a simple climate emulator that produced projections for IPCC AR6, under the SSP2-4.5 emissions scenario (11). FaIR's large ensemble is calibrated to match the historical record through 2022 while sampling the full range of uncertainty in ECS (55). We first make a minor revision to the FaIR ensemble's ECS distribution to match SW20 (*Materials and Methods*), and then we include the paleoclimate updates only to global-mean quantities in SW20 (i.e., excluding $\Delta\lambda$); this yields a median of 2.7 °C for end-of-century warming (relative to preindustrial) and a 66% *likely* range of 2.4 to 3.2 °C (90% CI: 2.1 to 3.5 °C). We then use our fully updated ECS

distribution from Fig. 4B with the FaIR model, which yields a median of 2.5 °C for end-of-century warming and substantially reduces uncertainty in the upper bound of warming projections, with a 66% *likely* range of 2.1 to 2.9 °C (90% CI: 1.9 to 3.2 °C) (Fig. 4C).

Pliocene pattern effects arise from changes in ice sheets, vegetation, and topography that amplify SST warming in the extratropics, in turn leading to cloud feedbacks that further amplify global warming. Recent work on the Last Glacial Maximum also found that ice sheets amplify extratropical SST cooling, similarly leading to positive cloud feedbacks (3). The modern climate feedback from CO₂ alone (in the absence of ice sheet, vegetation, and topography changes) is more stabilizing than the feedbacks associated with the Pliocene and LGM.

Updating global mean Pliocene and LGM temperatures based on the latest state-of-the-art reconstructions, while neglecting pattern effects, appears to suggest substantially higher estimates of climate sensitivity compared to SW20 (2) and IPCC AR6 (11). However, our results show that including spatial information from those same reconstructions leads to the opposite conclusion, such that paleoclimates now provide much stronger constraints on the modern climate's sensitivity to CO₂ and projected warming. We note that these 21st-century projections assume ice sheets will not be lost this century. An important corollary to our results is that a major shift in the modern warming pattern, e.g., caused by loss of the West Antarctic Ice Sheet (24, 28, 53), could

activate positive feedbacks on longer timescales in the modern climate similar to those that amplified global warming during the Pliocene.

Materials and Methods

AGCM Simulations. Following ref. 3, estimating paleoclimate $\Delta\lambda$ (Eq. 3) in AGCMs requires three simulations that differ only in their SST/SIC boundary conditions while all other forcings are constant at modern levels, similar to “amip-piForcing” simulations (6, 56).

The three categories of AGCM simulations are a) Preindustrial baseline, represented by the climatological mean of the Late Holocene (0 to 4 ka) (16), which integrates proxy constraints over a multimillennial interval when Earth’s energy budget was approximately in balance (57), and therefore estimates the mean preindustrial climate; b) $2\times\text{CO}_2$, for which we use the multimodel mean of quasi-equilibrium $2\times\text{CO}_2$ simulations in LongRunMIP (32); c) Pliocene, for which we use the various reconstructions described in the main text (Fig. 1 and SI Appendix, Figs. S1–S3). In CAM4 and CAM5, we also test the 5th and 95th percentiles of the plioDA ensemble (SI Appendix, Fig. S4); ensemble members are ranked by estimating λ_{Plio} with CAM4 Green’s functions (45). SST/SIC boundary conditions are prepared as described in ref. 3. We use plioDA’s SIC for ref. 13, as no SIC is provided by the latter; this approach is supported by similar ΔT_{Plio} in both reconstructions.

For each AGCM, we compute anomalies in simulations b) and c) relative to a). Simulations are 30 y, and we analyze means over the final 25 y for CAM4 (2° resolution), CAM5.3 (2°), CAM6.0 (2°) (58), and HadGEM3-GC3.1-LL (N96, 135 km) (59), or the final 30 of 31 y for GFDL-AM4.0 (C96, 100 km) (60). Results are included in SI Appendix, Tables S1 and S2. As described in ref. 3, we test sensitivity of $\Delta\lambda$ to the $2\times\text{CO}_2$ pattern by computing an alternative $\Delta\lambda_{150\text{y}}^{\text{Alt}}$, which uses the 150-y regression of abrupt CO_2 -forcing simulations in the parent coupled models corresponding to each AGCM instead of our $\lambda_{2\times\text{CO}_2}$. Each coupled model produces a distinct warming pattern over the 150-y period, thus $\Delta\lambda_{150\text{y}}^{\text{Alt}}$ samples uncertainty in CO_2 -warming patterns. This test confirms our finding of $\Delta\lambda < 0$ (SI Appendix, Tables S1 and S2) and produces ECS constraints that agree with our main result within 0.1°C (SI Appendix, Table S3). We decompose λ into component feedbacks (Planck, lapse rate, water vapor, surface albedo, shortwave cloud, and longwave cloud) using CAM5 radiative kernels (61), following ref. 44 (SI Appendix, Figs. S5–S8).

Constraining Modern Climate Sensitivity. Modern climate sensitivity is the steady-state response of global-mean T to doubling preindustrial CO_2 concentrations, including only the feedbacks acting on an approximate 150-y timescale, i.e., assuming fixed ice sheets and vegetation. This metric, called “effective climate sensitivity” to distinguish it from true equilibrium, is termed S in SW20 (2) and hereafter. To infer S from Pliocene evidence, we build on SW20’s equation of Pliocene energy balance by including the updates described below. (S percentile results are provided in SI Appendix, Table S3.)

$$\Delta T_{\text{Plio}} = \frac{-\Delta F_{\text{CO}_2} (1 + f_{\text{CH}_4}) - \Delta F_{\text{NonGHG}}}{\frac{\lambda_{2\times\text{CO}_2}}{1+\zeta} - \Delta\lambda} \quad [5]$$

- i) Our main update is incorporating Pliocene $\Delta\lambda$ as $\Delta\lambda \sim \mathcal{N}(\mu = -0.37, \sigma = 0.32) \text{ W m}^{-2} \text{ K}^{-1}$. We estimate μ and σ for $\Delta\lambda$ by combining the spread across AGCMs and reconstructions and using the approach described in detail in ref. 3 and briefly here. Our central estimate treats each AGCM and each Pliocene pattern as equally likely. To accomplish this equal weighting, we assume the spread in $\Delta\lambda$ from pattern uncertainty is similar between CAM4/CAM5, in which we ran simulations with each Pliocene pattern, and the other three models (CAM6, HadGEM3, and GFDL-AM4), in which we were only able to run simulations with three Pliocene patterns due to computing resources. Note that the assumption

of similar spreads across models is supported by the nearly identical 1σ values for $\Delta\lambda$ from CAM4 and CAM5 (SI Appendix, Table S2). For CAM4 and CAM5, we compute the differences between each pattern’s $\Delta\lambda$ and the plioDA best estimate of $\Delta\lambda$. We then add these differences to the plioDA best estimate of $\Delta\lambda$ in CAM6, HadGEM3, and GFDL-AM4, thereby estimating values of $\Delta\lambda$ for the patterns that were not run in those models. The result is a $\Delta\lambda$ distribution equally weighted across models and patterns. Drawing from this distribution, we execute 10^5 iterations of bootstrap resampling with $n = 23$ (representing the number of actual AGCM simulations estimating $\Delta\lambda$) to assess confidence in this estimate given the limited number of simulations informing the distribution. The resulting 95% CI on the mean value of $\Delta\lambda = -0.37 \text{ W m}^{-2} \text{ K}^{-1}$ is -0.50 to $-0.24 \text{ W m}^{-2} \text{ K}^{-1}$, and the 95% CI on the 1σ value of $0.32 \text{ W m}^{-2} \text{ K}^{-1}$ is 0.29 to $0.41 \text{ W m}^{-2} \text{ K}^{-1}$. See ref. 3 for further details.

- ii) Pliocene forcing is updated based on the recent estimate of effective radiative forcing from non-GHG sources (ΔF_{NonGHG}), including ice sheets, vegetation, and land-sea distribution (24). We assign $\Delta F_{\text{NonGHG}} \sim \mathcal{N}(1.7, 1.0) \text{ W m}^{-2}$, which assumes a 1σ uncertainty that approximately maintains the original SW20 uncertainty in total ΔF_{Plio} . For reference, total ΔF_{Plio} (numerator of Eq. 5) is $3.9 \pm 1.2 (1\sigma) \text{ W m}^{-2}$, with GHG forcing approximately 2.2 W m^{-2} . There is substantial uncertainty in the components of ΔF_{Plio} , which merit further study (18, 20, 42, 43, 62–65).
- iii) ΔT_{Plio} is updated from $3.0 \pm 1.0^\circ\text{C}$ (1σ) in SW20 to plioDA’s constraint of $\Delta T_{\text{Plio}} \sim \mathcal{N}(4.1, 0.6)^\circ\text{C}$ (12), which is supported by the estimate in ref. 13 of $3.9 \pm 1.1^\circ\text{C}$ (1σ).

From SW20 (2), the remaining parameters in Eq. 5 are CO_2 forcing of $\Delta F_{\text{CO}_2} = \Delta F_{2\times\text{CO}_2} \times \ln(\frac{[\text{CO}_2]}{284\text{ppm}}) / \ln(2)$, where $[\text{CO}_2] \sim \mathcal{N}(375, 25) \text{ ppm}$ and $\Delta F_{2\times\text{CO}_2} \sim \mathcal{N}(4.0, 0.3) \text{ W m}^{-2}$; a scaling factor for methane and N_2O forcing, $1 + f_{\text{CH}_4}$, with $f_{\text{CH}_4} \sim \mathcal{N}(0.4, 0.1)$; and a timescale transfer factor between quasi-equilibrium and the 150-y S timescale, $1 + \zeta$, to account for feedbacks becoming more positive at longer timescales (66), with $\zeta \sim \mathcal{N}(0.06, 0.2)$ based on LongRunMIP (32). Finally, modern climate sensitivity is $S = -\Delta F_{2\times\text{CO}_2} / \lambda_{2\times\text{CO}_2}$ (2).

We also use an alternative version of the $\Delta\lambda$ (described in i) estimated by comparing our paleoclimate AGCM simulations with feedbacks from 150-y regression of abrupt CO_2 -forcing simulations in the parent coupled models of each AGCM. Each coupled model produces a distinct warming pattern, thereby sampling uncertainty in the pattern of warming from CO_2 . With $\lambda_{150\text{y}}^{\text{CO}_2}$ representing the regression feedback, we estimate Pliocene $\Delta\lambda_{150\text{y}}^{\text{Alt}} = \lambda_{150\text{y}}^{\text{CO}_2} - \lambda_{\text{Plio}}$, and we use the same approach (described in i) to find Pliocene $\Delta\lambda_{150\text{y}}^{\text{Alt}} \sim \mathcal{N}(\mu = -0.44, \sigma = 0.40) \text{ W m}^{-2} \text{ K}^{-1}$. Because $\Delta\lambda_{150\text{y}}^{\text{Alt}}$ represents a comparison with the 150-y regression feedback rather than quasi-equilibrium simulations, the denominator of Eq. 5 becomes $(\lambda_{2\times\text{CO}_2} - \Delta\lambda_{150\text{y}}^{\text{Alt}}) / (1 + \zeta)$ when using $\Delta\lambda_{150\text{y}}^{\text{Alt}}$ instead of our standard $\Delta\lambda$. Note that the percentiles of the final S distribution agree within 0.1°C when using $\Delta\lambda_{150\text{y}}^{\text{Alt}}$ (SI Appendix, Table S3).

There are advantages to our formulation of the Pliocene energy balance (Eq. 5) compared to SW20’s Eq. 23. First, the Pliocene is now consistent with the LGM, as ΔF_{NonGHG} is now added directly rather than estimated by multiplying ΔF_{CO_2} by a scale factor, $1 + f_{\text{ESS}}$, representing Earth system sensitivity (1, 28). Second, f_{ESS} conflates forcings and feedbacks, and estimating f_{ESS} requires free-running coupled simulations that have inaccurate warming patterns (24). Instead of using f_{ESS} , our Eq. 5 separately includes effective radiative forcing, ΔF_{NonGHG} , from AGCM simulations with paleoenvironmental boundary conditions informed by proxies for ice extent, vegetation, and topography (24, 67), and paleoclimate pattern effects, from AGCM simulations with SST/SIC patterns constrained by data assimilation (3).

Climate sensitivity PDFs are summarized in *SI Appendix, Table S3*. We calculate likelihoods and PDFs for S using SW20's Bayesian framework (2). This framework quantitatively combines our findings with additional lines of evidence, and the methods can be continually developed in ongoing efforts (68, 69). Our findings would have the same directional impact on other assessments of ECS and modern warming (11, 70).

In *Fig. 4* and *SI Appendix, Table S3*, we show S with and without updates i), ii), and iii). For the LGM evidence in *Fig. 4B*, we include updated $\Delta T_{\text{LGM}} \sim \mathcal{N}(-6, 1)^\circ\text{C}$ and LGM $\Delta\lambda \sim \mathcal{N}(-0.37, 0.23) \text{ W m}^{-2} \text{ K}^{-1}$ (3). We also use $\lambda_{150\text{y}}^{\text{CO}_2}$ in *SI Appendix, Table S1* to estimate LGM $\Delta\lambda_{150\text{y}}^{\text{Alt}} \sim \mathcal{N}(\mu = -0.42, \sigma = 0.34) \text{ W m}^{-2} \text{ K}^{-1}$. While SW20's framework generally assumes lines of evidence are independent, our estimates of Pliocene and LGM pattern effects are interrelated. We use the same AGCMs, and the reconstruction methods are partially overlapping. To account for the relationship between Pliocene and LGM $\Delta\lambda$ estimates, we identify pairs of estimates that use similar reconstruction methods and the same AGCM (*SI Appendix, Table S4*). From these pairs, we estimate the Pearson correlation (r) and covariance for $\Delta\lambda$ to be $r = 0.56$ and $\text{cov} = 0.0123 [\text{W m}^{-2} \text{ K}^{-1}]^2$. For $\Delta\lambda_{150\text{y}}^{\text{Alt}}$, we estimate $r = 0.87$ and $\text{cov} = 0.0562 [\text{W m}^{-2} \text{ K}^{-1}]^2$. We account for the shared error covariance by drawing correlated values for LGM and Pliocene $\Delta\lambda$ from bivariate normal distributions. However, the S constraints are insensitive to the covariance, as our Full Update percentiles (*SI Appendix, Table S3*) change by less than 0.1°C if we assume zero covariance. This result aligns with the dependence tests in SW20, which also found relatively small impacts from codependencies (2).

We include results corresponding to SW20's robustness test, which assumes a uniform prior on S from 0 to 20°C instead of the baseline prior of uniform λ from -10 to $10 \text{ W m}^{-2} \text{ K}^{-1}$, in *SI Appendix, Table S3*. The robustness test yields a median of 3.1°C and 66% range of 2.6 to 3.8°C (90% CI: 2.3 to 4.6°C). As for our main result using the baseline prior, this represents a substantial narrowing of uncertainty compared to the robust ranges in SW20. For illustrative purposes, we also include posterior PDFs considering only the Pliocene evidence and assuming the uniform- S prior. The PDF from the Pliocene alone has a median of 3.8°C and 66% range of 2.4 to 7.2°C (90% CI: 1.9 to 12.9°C).

Projections of 21st-Century Warming. We analyze warming projections through 2100 under SSP2-4.5 (11) from the FaIR model v1.4.1, calibrated to match historical records as in IPCC AR6 but with updated constraints through 2022 (55). From FaIR, we have a large ensemble of global-mean temperatures from 1850–2100, and each member has an associated ECS. For each ensemble member, we compute the mean warming over 2081–2100 relative to the 1850–1900 mean. We then resample the ensemble with replacement to match the specified ECS distributions from SW20 and from our updated paleoclimate-constrained ECS. This resampling produces revised distributions of projected warming that are associated with the specified ECS distributions (*Fig. 4*).

1. PALAEOSENS Project Members, Making sense of palaeoclimate sensitivity. *Nature* **491**, 683–691 (2012).
2. S. C. Sherwood *et al.*, An assessment of Earth's climate sensitivity using multiple lines of evidence. *Rev. Geophys.* **58**, e2019RG000678 (2020).
3. V. T. Cooper *et al.*, Last Glacial Maximum pattern effects reduce climate sensitivity estimates. *Sci. Adv.* **10**, 9461 (2024).
4. K. C. Armour, C. M. Bitz, G. H. Roe, Time-varying climate sensitivity from regional feedbacks. *J. Clim.* **26**, 4518–4534 (2013).
5. T. Andrews, J. M. Gregory, M. J. Webb, The dependence of radiative forcing and feedback on evolving patterns of surface temperature change in climate models. *J. Clim.* **28**, 1630–1648 (2015).
6. J. M. Gregory, T. Andrews, Variation in climate sensitivity and feedback parameters during the historical period. *Geophys. Res. Lett.* **43**, 3911–3920 (2016).
7. P. Ceppi, J. M. Gregory, Relationship of tropospheric stability to climate sensitivity and Earth's observed radiation budget. *Proc. Natl. Acad. Sci. U.S.A.* **114**, 13126–13131 (2017).
8. T. Andrews, M. J. Webb, The dependence of global cloud and lapse rate feedbacks on the spatial structure of tropical pacific warming. *J. Clim.* **31**, 641–654 (2018).
9. K. D. Burke *et al.*, Pliocene and Eocene provide best analogs for near-future climates. *Proc. Natl. Acad. Sci. U.S.A.* **115**, 13288–13293 (2018).
10. E. de la Vega, T. B. Chalk, P. A. Wilson, R. P. Bysani, G. L. Foster, Atmospheric CO₂ during the Mid-Piacenzian Warm Period and the M2 glaciation. *Sci. Rep.* **10**, 11002 (2020).
11. P. Forster *et al.*, "2021: The Earth's energy budget, climate feedbacks, and climate sensitivity" in *Climate Change 2021: The Physical Science Basis. Contribution of Working Group I to the Sixth Assessment Report of the Intergovernmental Panel on Climate Change*, V. Masson-Delmotte *et al.*, Eds. (Cambridge Univ. Press, Cambridge, UK and New York, NY, 2021).

Data, Materials, and Software Availability. Model output and SST/SIC boundary conditions are available at <https://zenodo.org/records/18011042> (71). Pliocene reconstructions are available via refs. 12 and 13. Late Holocene reconstruction is available via ref. 16. Effective radiative forcings for the Pliocene and modern 2xCO₂ are available via ref. 24. Results for LGM pattern effects are available via ref. 3. LongRunMIP is available at <https://longrunmip.org>. CAM5 radiative kernels are available via ref. 61. Code for calculating ECS is available at <https://doi.org/10.5281/zenodo.3945276> (2).

ACKNOWLEDGMENTS. We acknowledge funding from a National Defense Science & Engineering Graduate Fellowship, U.S. Dept. of Defense (V.T.C.); NSF award OCE-2002276 (V.T.C., K.C.A., G.J.H., and M.T.D.); Heising Simons Foundation Award 2023-4715 (V.T.C. and G.J.H.); National Oceanic and Atmospheric Administration MAPP Program award NA200AR431039 (K.C.A., C.P., and M.T.D.); A Calvin Professorship in Oceanography (K.C.A.); NSF award OCE-2002398 (J.E.T. and M.B.O.); NSF award OCE-2002385 (C.P.); NSF award OCE-2002448 (N.J.B.); NSF award AGS-1844380 (N.J.B.); Met Office Hadley Centre Climate Programme funded by DSIT (T.A.); NSF award OCE-2103055 (R.F.); NSF award AGS-2238875 (R.F.). V.T.C. acknowledges computing support from Derecho (DOI: 10.5065/qx9a-pg09) and Casper (<https://ncar.pub/casper>) provided by the NSF National Center for Atmospheric Research, sponsored by NSF. We thank Yi Ming, Dan Amrhein, and Jiang Zhu for helpful discussions and NSF (No. 2238875) for funding a 2024 workshop on "Climate evolution from early Eocene to mid-Pliocene," which helped shape this work.

Author affiliations: ^aDepartment of Atmospheric and Climate Science, University of Washington, Seattle, WA 98195; ^bSchool of Oceanography, University of Washington, Seattle, WA 98195; ^cDepartment of Geosciences, University of Arizona, Tucson, AZ 85721; ^dDepartment of Atmospheric, Oceanic and Earth Sciences, George Mason University, Fairfax, VA 22030; ^eDepartment of Climate, Meteorology, and Atmospheric Sciences, University of Illinois at Urbana-Champaign, Champaign, IL 61820; ^fMet Office Hadley Centre, Exeter EX1 3PB, United Kingdom; ^gSchool of Earth and Environment, University of Leeds, Leeds LS2 9JT, United Kingdom; ^hCooperative Programs for the Advancement of Earth System Science, University Corporation for Atmospheric Research, Boulder, CO 80307; ⁱGeophysical Fluid Dynamics Laboratory, National Oceanic and Atmospheric Administration, Princeton, NJ 08540; ^jDepartment of Geosciences, University of Connecticut, Storrs, CT 06269; ^kDepartment of Geography, The University of Cambridge, Cambridge CB2 3EN, United Kingdom; and ^lDepartment of Atmospheric and Oceanic Sciences, University of California, Los Angeles, CA 90095

Author contributions: V.T.C. performed research; V.T.C. ran simulations in CAM4, CAM5, and CAM6; V.T.C. wrote the original draft; K.C.A. and G.J.H. supervised research; J.E.T. contributed paleoclimate reconstructions; K.C.A., G.J.H., J.E.T., N.J.B., and C.P. obtained funding; T.A. ran simulations in HadGEM3; W.D. ran simulations in GFDL-AM4; M.T.D. and R.F. contributed Pliocene forcing simulations; M.B.O. contributed paleoclimate reconstructions; and V.T.C., K.C.A., G.J.H., J.E.T., N.J.B., C.P., T.A., W.D., M.T.D., R.F., M.B.O., and Y.D. edited the paper.

The authors declare no competing interest.

This article is a PNAS Direct Submission. M.R. is a guest editor invited by the Editorial Board.

Copyright © 2026 the Author(s). Published by PNAS. This article is distributed under [Creative Commons Attribution-NonCommercial-NoDerivatives License 4.0 \(CC BY-NC-ND\)](https://creativecommons.org/licenses/by-nc-nd/4.0/).

12. J. E. Tierney *et al.*, Pliocene warmth and patterns of climate change inferred from paleoclimate data assimilation. *AGU Adv.* **6**, e2024AV001356 (2025).
13. J. D. Annan, J. C. Hargreaves, T. Mauritsen, E. McClymont, S. L. Ho, Can we reliably reconstruct the mid-Pliocene Warm Period with sparse data and uncertain models? *Clim. Past* **20**, 1989–1999 (2024).
14. J. E. Hansen *et al.*, Global warming in the pipeline. *Oxf. Open Clim. Change* **3**, kgad008 (2023).
15. J. E. Tierney *et al.*, Glacial cooling and climate sensitivity revisited. *Nature* **584**, 569–573 (2020).
16. M. B. Osman *et al.*, Globally resolved surface temperatures since the Last Glacial Maximum. *Nature* **599**, 239–244 (2021).
17. A. M. Seltzer *et al.*, Widespread six degrees Celsius cooling on land during the Last Glacial Maximum. *Nature* **593**, 228–232 (2021).
18. P. O. Hopcroft *et al.*, Polar amplification of Pliocene climate by elevated trace gas radiative forcing. *Proc. Natl. Acad. Sci. U.S.A.* **117**, 23401–23407 (2020).
19. U. Salzmann *et al.*, Challenges in quantifying Pliocene terrestrial warming revealed by data-model discord. *Nat. Clim. Change* **3**, 969–974 (2013).
20. H. Dowsett *et al.*, The PRISM4 (mid-Piacenzian) paleoenvironmental reconstruction. *Clim. Past* **12**, 1519–1538 (2016).
21. D. J. Lunt *et al.*, On the causes of mid-Pliocene warmth and polar amplification. *Earth Planet. Sci. Lett.* **321–322**, 128–138 (2012).
22. J. E. Tierney, A. M. Haywood, R. Feng, T. Bhattacharya, B. L. Otto-Bliesner, Pliocene warmth consistent with greenhouse gas forcing. *Geophys. Res. Lett.* **46**, 9136–9144 (2019).
23. L. E. Burton *et al.*, On the climatic influence of CO₂ forcing in the Pliocene. *Clim. Past* **19**, 747–764 (2023).
24. M. Dvorak *et al.*, Mid-Pliocene climate forcing, sea surface temperature patterns, and implications for modern-day climate sensitivity. *J. Clim.* **38**, 3037–3053 (2025).

25. J. E. Weiffenbach *et al.*, Unraveling the mechanisms and implications of a stronger mid-Pliocene Atlantic Meridional Overturning Circulation (AMOC) in PlioMIP2. *Clim. Past* **19**, 61–85 (2023).
26. R. Feng *et al.*, Past terrestrial hydroclimate sensitivity controlled by Earth system feedbacks. *Nat. Commun.* **13**, 1306 (2022).
27. S. Menemenlis, J. M. Lora, M. Lofverstrom, D. Chandan, Influence of stationary waves on mid-Pliocene atmospheric rivers and hydroclimate. *Glob. Planet. Change* **204**, 103557 (2021).
28. D. J. Lunt *et al.*, Earth system sensitivity inferred from Pliocene modelling and data. *Nat. Geosci.* **3**, 60–64 (2010).
29. G. J. Hakim *et al.*, The last millennium climate reanalysis project: Framework and first results. *J. Geophys. Res. Atmos.* **121**, 6745–6764 (2016).
30. R. Caballero, M. Huber, State-dependent climate sensitivity in past warm climates and its implications for future climate projections. *Proc. Natl. Acad. Sci. U.S.A.* **110**, 14162–14167 (2013).
31. I. Eisenman, K. C. Armour, The radiative feedback continuum from Snowball Earth to an ice-free hothouse. *Nat. Commun.* **15**, 6582 (2024).
32. M. Rugenstein *et al.*, LongRunMIP: Motivation and design for a large collection of millennial-length AOGCM simulations. *Bull. Am. Meteorol. Soc.* **100**, 2551–2570 (2019).
33. N. J. Steiger, J. E. Smerdon, E. R. Cook, B. I. Cook, A reconstruction of global hydroclimate and dynamical variables over the Common Era. *Sci. Data* **5**, 180086 (2018).
34. V. T. Cooper, G. J. Hakim, K. C. Armour, Monthly sea surface temperature, sea ice, and sea level pressure over 1850–2023 from coupled data assimilation. *J. Clim.* **38**, 5461–5490 (2025).
35. J. E. Tierney *et al.*, Advances in paleoclimate data assimilation. *Annu. Rev. Earth Planet. Sci.* **28**, 55 (2025).
36. D. E. Amrhein, G. J. Hakim, L. A. Parsons, Quantifying structural uncertainty in paleoclimate data assimilation with an application to the last millennium. *Geophys. Res. Lett.* **47**, e2020GL090485 (2020).
37. A. M. Haywood *et al.*, The Pliocene model intercomparison project phase 2: Large-scale climate features and climate sensitivity. *Clim. Past* **16**, 2095–2123 (2020).
38. N. J. Burls, A. V. Fedorov, What controls the mean east-west sea surface temperature gradient in the equatorial Pacific: The role of cloud albedo. *J. Clim.* **27**, 2757–2778 (2014).
39. E. Erfani, N. J. Burls, The strength of low-cloud feedbacks and tropical climate: A CESM sensitivity study. *J. Clim.* **32**, 2497–2516 (2019).
40. H. L. Ford *et al.*, Sustained mid-Pliocene warmth led to deep water formation in the North Pacific. *Nat. Geosci.* **15**, 658–663 (2022).
41. E. L. McClymont *et al.*, Lessons from a high-CO₂ world: An ocean view from 3 million years ago. *Clim. Past* **16**, 1599–1615 (2020).
42. A. Haywood *et al.*, Pliocene model intercomparison project phase 3 (PlioMIP3) - Science plan and experimental design. *Glob. Planet. Change* **232**, 104316 (2024).
43. J. R. Hall, M. S. Allison, M. T. Papadopoulos, D. N. Barford, S. M. Jones, Timing and consequences of Bering Strait opening: New insights from 40Ar/39Ar dating of the Barmur Group (Tjörnes beds), Northern Iceland. *Paleoceanogr. Paleoclimatol.* **38**, e2022PA004 (2023).
44. B. J. Soden *et al.*, Quantifying climate feedbacks using radiative kernels. *J. Clim.* **21**, 3504–3520 (2008).
45. Y. Dong, C. Proistosescu, K. C. Armour, D. S. Battisti, Attributing historical and future evolution of radiative feedbacks to regional warming patterns using a green's function approach: The preeminence of the western Pacific. *J. Clim.* **32**, 5471–5491 (2019).
46. M. W. Wara, A. C. Ravelo, M. L. Delaney, Permanent El Niño-like conditions during the Pliocene warm period. *Science* **309**, 758–761 (2005).
47. A. V. Fedorov *et al.*, The Pliocene paradox (mechanisms for a permanent El Niño). *Science* **312**, 1485–1489 (2006).
48. C. L. O'Brien *et al.*, High sea surface temperatures in tropical warm pools during the Pliocene. *Nat. Geosci.* **7**, 606–611 (2014).
49. C. Brierley, N. Burls, C. Ravelo, A. Fedorov, Pliocene warmth and gradients. *Nat. Geosci.* **8**, 419–420 (2015).
50. N. J. Burls, A. V. Fedorov, Wetter subtropics in a warmer world: Contrasting past and future hydrological cycles. *Proc. Natl. Acad. Sci. U.S.A.* **114**, 12888–12893 (2017).
51. B. L. Otto-Bliesner *et al.*, Amplified North Atlantic warming in the late Pliocene by changes in Arctic gateways. *Geophys. Res. Lett.* **44**, 957–964 (2017).
52. C. M. Brierley, A. V. Fedorov, Comparing the impacts of Miocene-Pliocene changes in inter-ocean gateways on climate: Central American Seaway, Bering Strait, and Indonesia. *Earth Planet. Sci. Lett.* **444**, 116–130 (2016).
53. J. E. Weiffenbach *et al.*, Highly stratified mid-Pliocene Southern Ocean in PlioMIP2. *Clim. Past* **20**, 1067–1086 (2024).
54. C. Wang *et al.*, Diagnosing the factors that contribute to the intermodel spread of climate feedback in CMIP6. *J. Clim.* **38**, 663–674 (2025).
55. C. Smith *et al.*, fair-calibrate v1.4.1: Calibration, constraining, and validation of the FaIR simple climate model for reliable future climate projections. *Geosci. Model. Dev.* **17**, 8569–8592 (2024).
56. T. Andrews, Using an AGCM to diagnose historical effective radiative forcing and mechanisms of recent decadal climate change. *J. Clim.* **27**, 1193–1209 (2014).
57. S. Shackleton, A. Seltzer, D. Baggenstos, L. E. Lisiecki, Benthic $\delta^{18}O$ records Earth's energy imbalance. *Nat. Geosci.* **16**, 797–802 (2023).
58. G. Danabasoglu *et al.*, The community earth system model version 2 (CESM2). *J. Adv. Model. Earth Syst.* **12**, e2019MS001916 (2020).
59. K. D. Williams *et al.*, The met office global coupled model 3.0 and 3.1 (GC3.0 and GC3.1) configurations. *J. Adv. Model. Earth Syst.* **10**, 357–380 (2017).
60. I. M. Held *et al.*, Structure and performance of GFDL's CM4.0 climate model. *J. Adv. Model. Earth Syst.* **11**, 3691–3727 (2019).
61. A. G. Pendergrass, A. Conley, F. M. Vitt, Surface and top-of-atmosphere radiative feedback kernels for CESM-CAM5. *Earth Syst. Sci. Data* **10**, 317–324 (2018).
62. G. R. Grant *et al.*, The amplitude and origin of sea-level variability during the Pliocene epoch. *Nature* **574**, 237–241 (2019).
63. N. Sahoo, T. Storelvmo, Testing the sensitivity of past climates to the indirect effects of dust. *Geophys. Res. Lett.* **44**, 5807–5817 (2017).
64. A. Dutton *et al.*, Sea-level rise due to polar ice-sheet mass loss during past warm periods. *Science* **349**, aaa4019 (2015).
65. N. Unger, X. Yue, Strong chemistry-climate feedbacks in the Pliocene. *Geophys. Res. Lett.* **41**, 527–533 (2014).
66. C. Proistosescu, P. J. Huybers, Slow climate mode reconciles historical and model-based estimates of climate sensitivity. *Sci. Adv.* **3**, e1602821 (2017).
67. J. Zhu, C. J. Poulsen, Last Glacial Maximum (LGM) climate forcing and ocean dynamical feedback and their implications for estimating climate sensitivity. *Clim. Past* **17**, 253–267 (2021).
68. K. Marvel, M. Webb, Towards robust community assessments of the Earth's climate sensitivity. *Earth Syst. Dyn.* **16**, 317–332 (2025).
69. S. C. Sherwood, C. E. Forest, Opinion: Can uncertainty in climate sensitivity be narrowed further? *Atmos. Chem. Phys.* **24**, 2679–2686 (2024).
70. D. Kaufman, V. Masson-Delmotte, Opinion: Distribute paleoscience information across the next Intergovernmental Panel on Climate Change reports. *Clim. Past* **20**, 2587–2594 (2024).
71. V. Cooper, Paleoclimate pattern effects help constrain climate sensitivity and 21st-century warming. Zenodo. <https://zenodo.org/records/18011042>. Deposited 3 January 2026.